



Contents lists available at ScienceDirect

Corrosion Science

journal homepage: www.elsevier.com/locate/corsci

The influence of applied stress rate on the stress corrosion cracking of 4340 and 3.5NiCrMoV steels in distilled water at 30 °C

S. Ramamurthy^{a,b,*}, A. Atrens^a^aDivision of Materials, University of Queensland, St. Lucia, Qld 4072, Australia^bSurface Science Western, The University of Western Ontario, London, Ont., Canada N6A 5B7

ARTICLE INFO

Article history:

Received 17 February 2009

Accepted 22 November 2009

Keywords:

A. High strength steel

Linearly Increasing Stress Test (LIST)

C. Stress corrosion cracking

ABSTRACT

Linearly Increasing Stress Tests conducted in 30 °C aerated distilled water using as-quenched 4340 and 3.5NiCrMoV turbine rotor steels indicated that stress corrosion cracking occurred at all applied stress rates for 4340 steel, whilst only at applied stress rates less than or equal to 0.002 MPa s⁻¹ for the turbine rotor steel. The crack velocity increased with increasing applied stress rate for both steels with the maximum crack velocity for 4340 steel corresponded to v_{II} in fracture mechanics tests in room temperature water. The fracture surface morphology was mixed mode consisting of intergranular and transgranular fracture regions.

© 2009 Elsevier Ltd. All rights reserved.

1. Introduction

Stress corrosion cracking (SCC) occurs when a susceptible material under stress is exposed to an appropriate environment. Crack growth occurs slowly until a critical crack length is reached; thereafter there is brittle fracture, which can be catastrophic [1–4]. Stress corrosion cracking of high strength steels has been widely studied, because of their importance to engineering applications [5–10]. Also, comprehensive research of the root causes has been an on-going effort [1,11–14]. The present study follows on from the previous investigation [15] into the effect of the applied stress rate on the stress corrosion cracking of two high strength steels in distilled water at 90 °C, and the interested reader is referred to that paper for a discussion of the possible effects of the applied stress rate. In summary, in the simplest anodic dissolution mechanism, the crack tip strain rate maintains a bare crack tip and the crack can advance by chemical dissolution of the crack tip metal. In SCC caused by hydrogen, the crack tip strain rate role may be to maintain bare metal to allow corrosion to occur liberating hydrogen by the cathodic reaction; alternatively the role may be to maintain a bare surface to allow hydrogen entry into the metal. The temperature 90 °C represents a high temperature for the stress corrosion cracking of high strength steels, where it has been suggested [15–17] that the cracking mechanism involves anodic dissolution. The stress corrosion crack velocity at 90 °C was dependent on the applied stress rate and increased with increasing applied

stress rate. Stress corrosion crack initiation was controlled both by the development of corrosion pits on the specimen surface and by the crack tip strain rate, although the crack tip strain rate had more influence on initiation than the development of corrosion pits. The prior research used the Linearly Increasing Stress Test (LIST) methodology [18–26]. Subsequently, SCC initiation for 4340 in distilled water was studied [27] using stressed samples in an environmental scanning electron microscope (ESEM); the observations indicated that there were surface films as expected from the Pourbaix diagram, that these were at least partially protective, and these were involved in the initiation of SCC.

The present research also used LIST to study the stress corrosion cracking of the same two high strength steels at much lower temperatures. Slow strain rate type tests have not been previously used to study the stress corrosion cracking of high strength steels in room temperature distilled water, although there have been fracture mechanics type studies [16,28–30]. The present study is aimed at the scientific understanding of the stress corrosion cracking mechanism of high strength steels and in particular the role of the applied stress rate.

2. Experimental procedure

This study used as-quenched 4340 steel and 3.5NiCrMoV turbine rotor steel, which were the same as used in the previous study [15]. The composition of these steels is presented in Table 1. Cylindrical tensile specimens, 8.5 mm in diameter and 80 mm in length, with a gauge section of 4.0 mm diameter and 15 mm in length were machined from respective steel blocks. All 4340 steel specimens were austenitized at 860 °C in high purity nitrogen for 1 h

* Corresponding author. Address: Surface Science Western, The University of Western Ontario, London, Ont., Canada N6A 5B7. Tel.: +1 519 661 2173; fax: +1 519 661 3709.

E-mail address: sramamur@uwo.ca (S. Ramamurthy).

Table 1
Composition of the steels used in this study.

Steel	Composition (wt.%)								
	C	Ni	Cr	Mo	V	Mn	P	Si	S
4340	0.35	1.47	1.5	0.25	0.01	0.5	0.017	0.35	0.025
3.5NiCrMoV	0.23	3.05	1.9	0.65	0.07	0.45	0.011	–	0.009

and quenched into oil. Similar procedure was followed for the 3.5NiCrMoV steel specimens. Batch heat-treatment ensured that the starting microstructure was the same for all specimens for each steel composition. This heat treatment resulted in a fully martensitic microstructure in both the steels with a prior austenite grain size of 20 μm . The microstructure of the as-quenched 3.5NiCrMoV rotor steel is described by Gates et al. [31]. The yield strength of the 4340 steel was 1700 MPa and of the rotor steel was 1270 MPa. After heat-treatment, the specimens were mounted in a lathe and the gauge section was polished through successive silicon carbide papers to 800 grit finish. Identical polishing condition, including the lathe speed, was employed for the preparation of all samples. Further, the gauge section of the specimens were examined under optical microscopy after the polishing processes to ensure that the gauge section morphology was uniform and did not contain any coarse scratches or other surface aberrations that could act as crack initiation sites. The samples were then degreased in an ultrasonic cleaner with technical grade hexane solution, rinsed with distilled water and immediately loaded in the LIST apparatus.

The LIST apparatus is described elsewhere [18,22,23–26]. Each machine consists of a lever beam. The specimen loading train is on one side of the lever beam and the other arm contains a known movable weight. Movement of the weight, driven by a synchronous motor, from its equilibrium position causes a proportional load on the specimen. The loading on the specimen is reported in terms of the engineering stress. Using synchronous motors of different speeds allows various applied stress rates. Nine stress rates, ranging from 0.0002 to 26 MPa s^{-1} were used in this study.

All experiments were carried out in aerated distilled water at 30 °C at the open circuit corrosion potential. Tests were conducted at 30 °C rather than at room temperature to ensure minimal variation in temperature. Once the desired temperature was reached, an hour was allowed for stabilisation before the stress rate was applied. After fracture, the specimen was removed from the cell, washed with distilled water and dried. The fracture stress, σ_f , was calculated from the position of the load at specimen fracture and the initial cross-section area of the specimen. The fracture surfaces were examined in a scanning electron microscope (SEM).

Two identical samples were tested at each applied stress rates where stress corrosion cracking was observed. The exception being the experiments at very low applied stress rates (0.00034 and 0.0002 MPa s^{-1}) where only one sample was tested. This is because of the duration of these tests which took two months or longer to complete.

As presented previously [18,20,22,23–26], the threshold stress, σ_{th} , for stress corrosion cracking was determined using a potential drop technique. During the LIST tests, a 5-A stabilised d.c. current (from a BWD model 245A power supply) was applied to the specimen and the resulting potential drop across the specimen was plotted as a function of the applied stress. The threshold stress was measured to be the stress at which there was a change in the slope in the potential drop versus applied stress plot, corresponding to the decrease in the cross-sectional area of the gauge section due to crack propagation. A CDP-10 linear displacement transducer (manufactured by Tokyo Sokki Kenkyujo Ltd) was attached to the loading arms to measure the displacement of the

specimen. This displacement was calibrated to give an output proportional to the specimen strain. The strain rate at the threshold stress was in each case determined from the slope of the strain versus time plot at the threshold stress (the threshold stress itself was evaluated from the potential drop measurements).

Assuming the stress corrosion cracks grow at a constant rate between σ_{th} and σ_f , the average crack growth rate, v , was calculated from the following equation, where a is the maximum crack length observed on the fracture surface after the test and $\dot{\sigma}$ is the applied stress rate [15]:

$$v = \frac{a\dot{\sigma}}{\sigma_f - \sigma_{th}} \quad (1)$$

The precision in the LIST tests were as follows. The total error on the load on the specimen was determined to be less than $\pm 1\%$ for loads of 1000 N and less than $\pm 0.14\%$ for higher loads [18]. The loading rate, determined by the speed of the synchronous motor, was determined to be accurate to $\pm 1\%$ [18]. The precision in the potential drop measurements was $\pm 0.1 \mu\text{V}$ and potential drop values were measured at every second for higher applied stress rates and at every few minutes for the very low applied stress rates. The precision in the temperature control was better than $\pm 1 \text{ }^\circ\text{C}$. Finally, the error in the crack length measurements was determined to be $\pm 0.1 \text{ mm}$ [18].

3. Experimental results

3.1. Potential drop measurements

Figs. 1 and 2 present typical potential drop curves; the potential drop is plotted against the applied stress for 4340 steel and the 3.5NiCrMoV turbine rotor steel, respectively, subjected to the LIST in distilled water at the free corrosion potential. Each number on Figs. 1 and 2 identifies the potential drop data for the test with that same number in Figs. 3 and 4, respectively. The curves numbered 4 and 5 in Fig. 2 each represent a specimen, for which there was ductile fracture and there was no change in the slope of the potential drop – applied stress plot until the yield stress was reached, after which the slope increased sharply due to plastic deformation. All the other curves in Fig. 2 and all the curves in Fig. 1 exhibited an increase in the slope of the potential drop – applied stress curve corresponding to the initiation of stress corrosion cracking. This

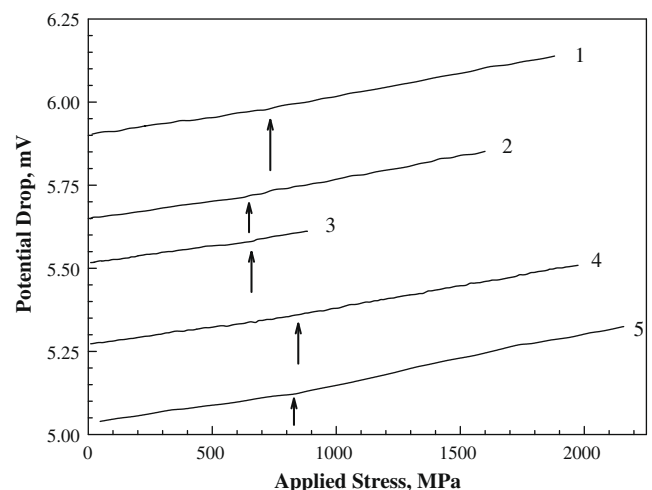


Fig. 1. A plot of the potential drop as a function of the applied stress for representative tests with as-quenched 4340 steel. Numbers 1–5 represent the corresponding data points in Fig. 3. The arrows represent the point where a change in slope was observed in the potential drop plot.

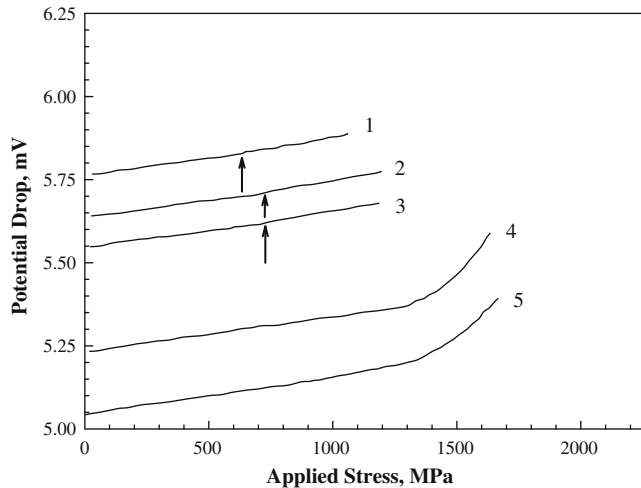


Fig. 2. A plot of the potential drop as a function of the applied stress for typical experiments with as-quenched rotor steel specimens. Numbers 1–5 represent the corresponding data points in Fig. 4. The arrows represent the point where a change in slope was observed in the potential drop plot. The curves numbered 4 and 5 each represent a specimen for which there was ductile fracture and there was no change in the slope of the potential drop – applied stress plot until the yield stress was reached, after which the slope increased sharply due to plastic deformation.

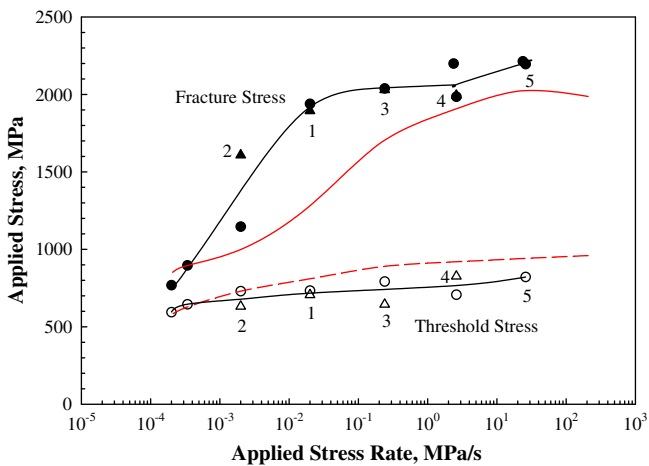


Fig. 3. A plot of fracture stress (closed symbols) and threshold stress (open symbols) plotted as a function of the applied stress rate for as-quenched 4340 steel in distilled water at 30 °C. The numbers 1–5 correspond to the potential drop plots shown in Fig. 1. The data from 90 °C water tests are shown as red lines [15]. (For interpretation of the references to color in this figure legend, the reader is referred to the web version of this paper.)

point was has been marked by an arrow for each curve in both figures and was identified as the threshold stress.

3.2. Fracture stress and threshold stress

The threshold stress and the fracture stress for as-quenched 4340 in aerated distilled water at 30 °C are plotted in Fig. 3 as a function of applied stress rate. The solid lines represent the polynomial regression fit for the data presented in this figure. There was stress corrosion cracking at all the stress rates shown in the figure, though some specimens tested at stress rates of 2.08 and 20.8 MPa s⁻¹ failed in a ductile manner. The fracture stress decreased slightly with decreasing applied stress rate until 0.02 MPa s⁻¹ and decreased significantly with further decrease in

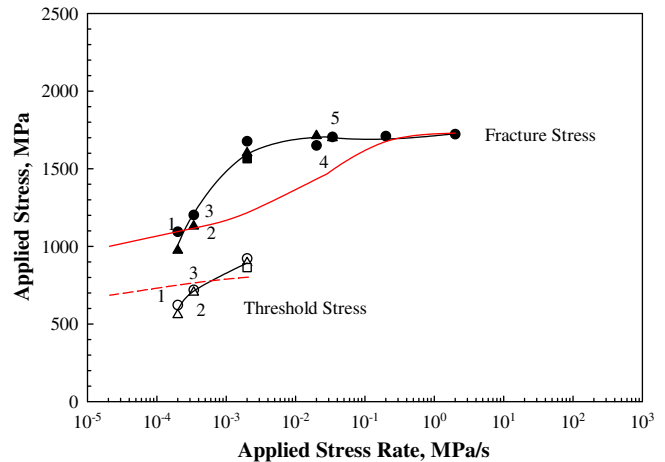


Fig. 4. A plot of fracture stress (closed symbols) and threshold stress (open symbols) plotted as a function of the applied stress rate for as-quenched 3.5NiCrMoV steel in distilled water at 30 °C. The numbers 1–5 correspond to the potential drop plots shown in Fig. 2. The data from 90 °C water tests are shown as red lines [15]. (For interpretation of the references to color in this figure legend, the reader is referred to the web version of this paper.)

the applied stress rate. At low applied stress rates, the fracture stress approached the threshold stress and was about one third of the fracture stress at higher stress rates. The threshold stress data, represented by the open symbols, is also plotted in this figure. The data and the polynomial fit indicated that the threshold stress decreased slightly with decreasing applied stress rate. As mentioned previously, at low applied stress rates, the threshold stress was one third of the fracture stress value at higher applied stress rates. For comparison, the data from the previous study in 90 °C water is also presented in this figure: the solid and dotted red lines present the trends lines for the fracture stress and threshold stress, respectively, at 90 °C from the prior study [15]. Comparison of the fracture stress values between the 30 °C and 90 °C tests indicates that the fracture stress was slightly greater at corresponding stress rates for the specimens tested in 30 °C water. At low applied stress rates, the fracture stresses were similar for the 30 and 90 °C tests. Moreover, the applied stress rate at which the fracture stress started decreasing significantly was lower for the 30 °C test (0.02 MPa s⁻¹) compared to that for the tests in water at 90 °C (0.2 MPa s⁻¹).

There were also differences in the threshold stress between the 30 °C and 90 °C tests. The threshold stress decreased slightly with decreasing applied stress rate for the tests conducted in 30 °C water. This is in contrast to the 90 °C data (presented by the dotted red lines), in which the threshold stress remained constant at higher applied stress rates and decreased with decreasing applied stress rate at lower applied stress rates. Also, at lower applied stress rates, the magnitude of the threshold stress was the same as that for tests conducted in 90 °C water at corresponding applied stress rates and were about one third of the yield strength.

Fig. 4 presents the results for as-quenched 3.5NiCrMoV rotor steel. There was no stress corrosion cracking in water at stress rates higher than 0.002 MPa s⁻¹ and the fracture stress remained essentially constant with increasing applied stress rate. There was stress corrosion cracking at stress rates equal to or less than 0.002 MPa s⁻¹ and the fracture stress significantly decreased with decreasing applied stress rate. Where there was stress corrosion cracking, the threshold stress decreased with decreasing applied stress rate.

The data from the 90 °C tests for the as-quenched 3.5NiCrMoV steel are plotted as red lines for comparison purposes. At 90 °C,

there was stress corrosion cracking at most applied stress rates, except for the two highest stress rates. The fracture stress decreased with decreasing applied stress rate. This trend was similar to that for the 4340 steel as shown in Fig. 3. When there was no stress corrosion cracking at the higher applied stress rates in the 30 °C test, the fracture stress remained constant close to the ductile fracture stress; the fracture stress decreased with decreasing applied stress rate when there was stress corrosion cracking. In addition, trends in the threshold stress were also different between the 30 and 90 °C test. The threshold stress in the 30 °C test decreased with decreasing applied stress rate, while it remained essentially constant with the applied stress rate in the 90 °C tests.

3.3. Crack tip strain rate versus applied stress rate

The crack tip strain rates were calculated using two approaches as described in the prior paper [15]. The first approach was based on the assumption of a plane strain state acting at the crack tip [32]. Congleton et al. [32] have shown that the crack tip strain rate $\dot{\epsilon}_c$ at a distance x (in meters) from the tip of a growing crack in an ideally plastic solid under plane strain, small scale yielding conditions, large scale yielding and fully plastic conditions, is given by [32]:

$$\dot{\epsilon}_c = \frac{\alpha L}{nx} (\dot{\epsilon}_m - \dot{\epsilon}_{NC}) + \frac{\beta \sigma_y \nu}{Ex} \left[\ln \frac{0.2E(\Delta - \Delta_{NC})}{n\sigma_y x} \right] \quad (2)$$

where $a (=0.5)$ is a constant, which was determined from the finite element analysis to be the same for stationary and growing cracks. L is the gauge length in meters, n is the number of circumferential cracks observed on the gauge section, $\dot{\epsilon}_m$ and $\dot{\epsilon}_{NC}$ are the strain rates acting on the specimen and on an uncracked gauge length, respectively, β is a constant with a value equal to 5.083 for a Poisson's ratio, ν , equal to 0.3, σ_y is the yield strength of the steel in MPa, ν is the crack velocity in ms^{-1} , E is the Young's modulus in MPa, Δ and Δ_{NC} are the total displacement in meters for the cracked and the uncracked gauge length, respectively. The total elongation Δ and the total crack mouth opening displacement Δ_c , which may correspond to the crack opening displacement (after Congleton et al. [32]) were measured on several LIST specimens tested at various applied stress rates and the average values at each stress rate are presented in Table 2. Table 2 shows that the average Δ_c values were 1.09×10^{-4} and 1.44×10^{-4} m for 4340 and the rotor steel, respectively. Similar to the 90 °C water results, the Δ/Δ_c ratio increased with decreasing applied stress rate. Table 2 implies that the mean values of $\dot{\epsilon}_{NC}$ are 0.65 $\dot{\epsilon}_{ext}$ and 0.56 $\dot{\epsilon}_{ext}$ for 4340 and turbine rotor steels, respectively. Substituting these values, together with the values of α , β , the yield strength of the steels, the Young's modulus $E = 210000$ MPa and choosing $x = 5 \times 10^{-5}$ m as an arbitrary choice (the value of x varies between 1×10^{-5} and 1×10^{-4} m Congleton et al. [32]) Eq. (2) becomes:

$$\dot{\epsilon}_c = \left[\frac{51}{n} \right] \dot{\epsilon}_{ext} + 823a \ln \left[\frac{52}{n} \right] \quad (3)$$

$$\dot{\epsilon}_c = \left[\frac{66}{n} \right] \dot{\epsilon}_{ext} + 615a \ln \left[\frac{94.6}{n} \right] \quad (4)$$

for 4340 and turbine rotor steels, respectively.

The second approach for calculating the crack tip strain rate was based on the assumption of plane stress acting at the crack tip. Development of the model and the equations employed for the calculation of the crack tip strain rate were presented previously [11]. This model assumes plasticity at the crack tip and a crack tip stress equal to the yield strength. Moreover, as discussed in the previous paper [15], this model is partially based on the analysis of slow strain rate stress corrosion cracking data by Silcock [33]. As de-

Table 2

Average values of the total elongation Δ and the total crack mouth opening displacement Δ_c measured at various applied stress rates for as-quenched 4340 steel and turbine rotor steel tested in aerated distilled water at 30 °C.

Steel	Applied stress rate, MPa s ⁻¹	No. of cracks observed along the gauge length, n	Total elongation Δ ($\times 10^{-3}$ m)	Total crack mouth displacement Δ_c ($\times 10^{-3}$ m)	Δ_c/Δ
4340	26.0000	1	0.49	0.11	0.224
	2.6000	1	0.39	0.09	0.230
	0.24000	1	0.34	0.08	0.235
	0.02080	1	0.265	0.10	0.377
	0.00208	2	0.295	0.125	0.423
	0.00034	4	0.27	0.14	0.519
	0.00020	4	0.26	0.12	0.46
	Mean		0.33	0.109	0.352
Rotor	0.00208	1	0.303	0.133	0.440
	0.00034	2	0.33	0.135	0.412
	0.00020	3 or 4	0.345	0.165	0.477
	Mean		0.326	0.144	0.442

scribed in the model [15], the total measured strain ($\dot{\epsilon}_m$) is equal to the sum of the strain on the uncracked gauge length ($\dot{\epsilon}_{uncracked}$) and the strain associated with stress corrosion cracks ($\dot{\epsilon}_{cracked}$). Assuming plasticity at the crack tip [$\sigma = K\epsilon^n$ where K is a constant and n is the strain hardening coefficient] and determining the strain due to stress corrosion cracks and that from the uncracked gauge length [15], the equation for crack tip strain rate becomes:

$$\dot{\epsilon}_c = \left[\frac{L[\dot{\epsilon}_m - \dot{\epsilon}_u + \frac{m\Delta_c \dot{\epsilon}_u}{L}]}{nm\Delta_c \sigma_y} \right] \dot{\sigma} \quad (5)$$

A point worth noting is that, unlike Eqs. (3) and (4), the Eq. (5) does not contain either the crack velocity or the macroscopic strain rate for the calculation of the crack tip strain rate. However, both the $\dot{\epsilon}_m$ and Δ_c terms are affected by the stress corrosion crack velocity and the stress corrosion crack depth terms and generally increase with an increase in either term. The macroscopic strain rate term is accounted for by the applied stress rate, which controls the macroscopic strain rate in the present study.

The crack tip strain rate values calculated from both approaches are plotted in Fig. 5. In addition, two more strain rates have also been plotted in this figure. The first one is the lowest line on this figure, which corresponds to the expectation from $\dot{\epsilon} = \dot{\sigma}/E$, where the strain rate has been calculated from the applied stress rate on the assumption of elastic deformation. This data is represented by small dark circles in this figure. The second plot is the measured macroscopic strain rate, measured at the threshold stress as a function of applied stress rate. This data has been represented by full circles and triangles for the 4340 and rotor steels, respectively. This strain rate was determined as the slope of the macroscopic strain versus time data. The solid lines in this figure represent the least square fit of the strain rate data to a relationship of the form $\dot{\epsilon} = A1\dot{\sigma}^{m1}$, where $\dot{\epsilon}$ is the relevant strain rate, $A1$ is a constant, $m1$ is the slope of the corresponding straight line and $\dot{\sigma}$ is the applied stress rate. For the measured macroscopic strain rate data (measured at the threshold stress), the least square fit yields the following relationship. The fit parameters are presented in Table 3.

$$\dot{\epsilon}_m = 9.5 \times 10^{-6} \dot{\sigma}^{1.01} \quad (6)$$

The open triangles and the crosses represent the crack tip strain rate calculated using Eqs. (3) and (4) based on the methodology described by Congleton et al. [32] Least square fit of this data (solid lines through the symbols) yields the following relationship (Table 3):

$$\dot{\epsilon}_c = 1.7 \times 10^{-3} \dot{\sigma}^{0.85} \quad (7)$$

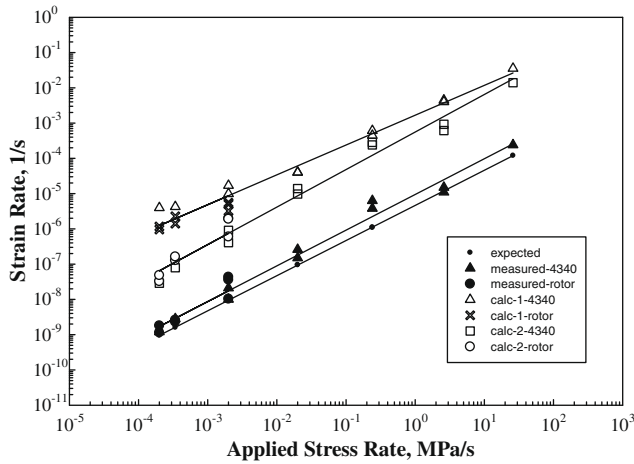


Fig. 5. Plots of strain rate as a function of the applied stress rate. The lowest line corresponds to the expectation that the strain rate can be calculated from the applied stress rate on the assumption of elastic deformation. The full triangles and circles represent measurements of the macroscopic specimen strain rate, measured at the threshold stress as a function of the applied stress rate. The open symbols represent the crack tip strain rate evaluated based on the best existing literature approaches. The open triangles and crosses have been calculated using, respectively, Eqs. (3) and (4) using the method of Congleton et al. [32]. The open squares and circles have been calculated based on the approach of Silcock [33] using Eq. (5). The least square fit parameters are presented in Table 2.

Table 3
Parameters for the least square fit of the data reported in this study and the results from 90 °C water experiments [15].

Data to be fitted	Relationship	Parameters for 30 °C water		Parameters for 90 °C water [15]	
		Constant A	Slope m	Constant A	Slope m
Measured strain rate versus applied stress rate	$\dot{\epsilon}_m = A\sigma^m$	9.5×10^{-6}	1.01	1.9×10^{-5}	1.02
Calculated crack tip strain rate versus applied stress rate (calculation 1)	$\dot{\epsilon}_c = A1\sigma^{m1}$	1.7×10^{-3}	0.85	3.4×10^{-3}	0.84
Calculated crack tip strain rate versus applied stress rate (calculation 2)	$\dot{\epsilon}_c = A1\sigma^{m1}$	5.6×10^{-4}	1.06	5.9×10^{-4}	1.05
Stress corrosion crack velocity versus applied stress rate	$v = A2\sigma^{m2}$	3.4×10^{-4}	0.78	7.6×10^{-7}	0.78
Stress corrosion crack velocity versus measured strain rate	$v = A3\dot{\epsilon}_m^{m3}$	3.2×10^{-3}	0.73	1.4×10^{-2}	0.98
Stress corrosion crack velocity versus calculated crack tip strain rate (calculation 1)	$v = A4\dot{\epsilon}_c^{m4}$	1.4×10^{-4}	0.89	1.8×10^{-4}	0.74
Stress corrosion crack velocity versus calculated crack tip strain rate (calculation 2)	$v = A4\dot{\epsilon}_c^{m4}$	1.59×10^{-4}	0.73	1.6×10^{-4}	0.94

The open squares and the circles have been based on the approach from Silcock [33] as described above. Least square fit of this data (solid lines through the symbols) yields the following relationship (Table 3):

$$\dot{\epsilon}_c = 5.6 \times 10^{-4} \sigma^{1.06} \tag{8}$$

This figure indicates that the crack tip strain rate was approximately 200 times greater than the measured macroscopic specimen strain rate. At low values of applied stress rate there are significant differences in the crack tip strain rates calculated by the two approaches, while at higher applied stress rates, both values tend to approach each other. The ratio $\dot{\epsilon}_c/\dot{\epsilon}_m$ has values between 100 and 300 at higher applied stress rates and about 2000 at low applied stress rates for calculation 1 (Eqs. (3) and (4)) and 50–65 at higher applied stress rates and about 40–20 at lower applied stress rates for calculation 2 (Eq. (5)). The magnitude of these ratios is similar to the data from 90 °C water experiments [15]. Moreover, the parameters for the least square fit indicate that the external strain rate data had a slope of 1.01, whereas the slope of the least square fit lines for the crack tip strain rate data are 0.85 and 1.06, respectively. Comparison of this data to the 90 °C results [15] (Table 3) indicate that the slopes for 30 °C measurements are similar to those for 90 °C measurements. The close correlation in the crack tip strain rates for tests conducted in 90 °C and 30 °C water suggests that the crack tip strain rate was controlled by the applied stress rate or through the external strain rate produced by the applied stress rate in both tests.

The values of the ratio $\dot{\epsilon}_c/\dot{\epsilon}_m$ are greater than that reported in literature for the stress corrosion cracking of austenitic stainless steels in high temperature water, where an average of 10 cracks were observed in the specimen gauge section [34–37]. In our experiments, only a single crack was observed on the gauge section at higher applied stress rates and two to four cracks were observed at lower applied stress rates. Perhaps, the smaller number of cracks could have resulted in the much greater crack tip strain rates observed in this study.

Finally, the crack tip strain rates determined in this study are within the range for 3.5NiCrMoV steels in which stress corrosion cracking was observed [7] for CERT tests in water. In their study, SCC was observed when the strain rates were between 5×10^{-8} and $5 \times 10^{-7} \text{ s}^{-1}$ and ductile fracture was observed when the strain rates were of the order of 10^{-6} – 10^{-5} s^{-1} . In our study, SCC was observed in this steel when the strain rates were of the order of 10^{-9} – 10^{-8} s^{-1} . Our measurements were conducted in 30 °C water, while the lowest temperature was tested in their study was 50 °C, which could explain the discrepancy at the higher limit of the measured strain rates at which SCC was observed.

3.4. Crack velocity versus applied stress rate

Fig. 6 presents the average stress corrosion crack velocity data from both steels plotted as a function of the applied stress rate. The crack velocity has been evaluated using Eq. (1). Fig. 6 shows that the crack velocity was dependent on the applied stress rate; the dependence was more pronounced for 4340. With increasing applied stress rate, the crack velocity increased until the maximum crack velocity was reached. This maximum crack velocity for 4340 was similar to the plateau crack velocity observed in the fracture mechanics tests conducted at 30 °C water by Magdowski [16,28], whereas the maximum crack velocity observed for the turbine rotor steel was two orders of magnitude lower than that reported by Magdowski [16,28] for this steel in 30 °C water. Both 4340 and the turbine rotor steel exhibited similar crack velocities (within an order of magnitude) at corresponding applied stress rates, which indicates that the crack velocity was independent of the steel

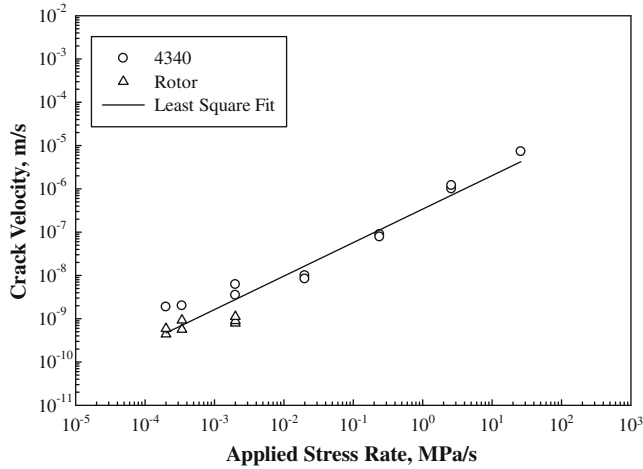


Fig. 6. Average crack velocity plotted as a function of applied stress rate for both steels. The least square fit parameters are presented in Table 2.

(composition and strength) and dependent only on the applied stress rate. Fig. 6 also shows that, at any applied stress rate, there is a scatter in stress corrosion crack velocity by about a factor of two.

The straight line in Fig. 6 is the least square fit of the data to the relation $v = A2\dot{\sigma}^{m2}$, with the slope $m2$ equal to 0.78 and $A2$ is equal to 3.4×10^{-7} , a constant independent of applied stress rate. The fit parameters are also presented in Table 3. A similar value of slope (0.73) was obtained when the average crack velocity was plotted against the external strain rate measured at the threshold stress, $\dot{\epsilon}_m$, and fitted to the relation $v = A3\dot{\epsilon}_m^{m3}$ (Table 3) which suggests that the external strain rate was dependent on the applied stress rate.

Fig. 7 presents the least square fit of the stress corrosion crack velocity versus the applied stress rate for both 30 °C water and 90 °C water experiments. Fig. 7 shows that the slopes of the least square fit lines for the data at both temperatures were nearly identical, though the stress corrosion cracking velocity at 90 °C was slightly higher than at 30 °C at corresponding applied stress rates. This observation indicates that for both 30 and 90 °C tests, the effect of the applied stress rate on stress corrosion cracking of these steels was the same at both temperatures and the crack velocity was dependent on the applied stress rate.

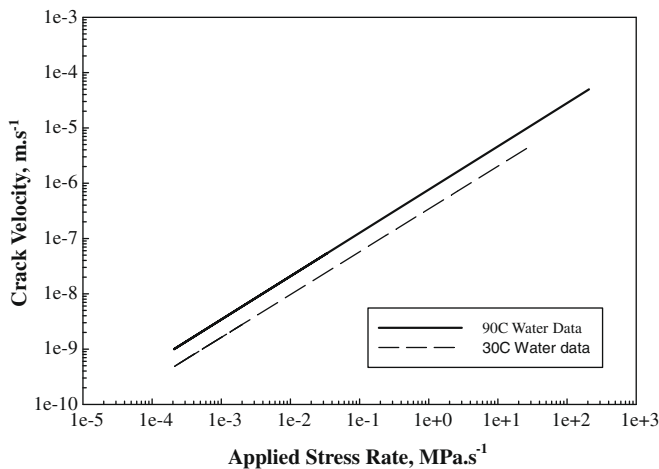


Fig. 7. Linear square fit plots of average stress corrosion crack velocity as a function of applied stress rate for 30 °C water (dash line) and 90 °C water (solid line) for both steels. The least square fit parameters are presented in Table 2.

3.5. Crack velocity versus crack tip strain rate

Fig. 8 presents the stress corrosion crack velocity plotted against the crack tip strain rate, calculated using the two approaches as discussed above. The closed symbols represent the data from the first approach (Eqs. (3) and (4)); the open symbols represent the second approach (Eq. (5)). The solid lines represent the least square fit of the data to the equation $v = A4\dot{\epsilon}_c^{m4}$, where $m4$ is the exponent and $A4$ is the constant. The fit parameters are presented in Table 3. The exponent ($m4$) values are 0.89 for approach 1 (Eqs. (3) and (4)) and 0.73 for approach 2 (Eq. (5)).

The data presented in Fig. 8 show that the crack velocity was dependent on the crack tip strain rate and increased with increasing crack tip strain rate. Both the 4340 and the turbine rotor steel specimens had similar crack velocities at corresponding crack tip strain rates. This observation is similar to the trends presented in the crack velocity versus the applied stress rate plot presented in Fig. 7. In fact, the exponents in Figs. 7 and 8 (as shown in Table 3) are similar in value. This suggests that the crack tip was under plane stress state for most of the test and was proportional to the applied stress rate.

Fig. 9 presents the least square fit of the 30 °C and 90 °C water data and this plot shows the comparison of the trends observed in the 30 °C and 90 °C water experiments. This figure and Table 3 show that the exponents (slopes) were similar at both temperatures, thus indicating that the effect of the applied stress rate on the stress corrosion crack velocity was similar at these two temperatures and the stress corrosion crack velocity was dependent on the applied stress rate through the crack tip strain rate.

3.6. Fractography

Figs. 10 and 11 present representative secondary scanning electron micrographs for the 4340 steel and rotor steel at various applied stress rates. Micrographs at five different applied stress rates are presented in Fig. 10 for 4340. Fig. 11 presents the micrographs at the applied stress rates where there was stress corrosion cracking in the rotor steel. These micrographs indicate that the fractography was similar for all applied stress rates and for both steels. The applied stress rate did not influence the fracture morphology. The micrographs indicated that the fracture morphology was a mixed mode consisting of some intergranular fracture with a large amount of transgranular fracture with a significant amount

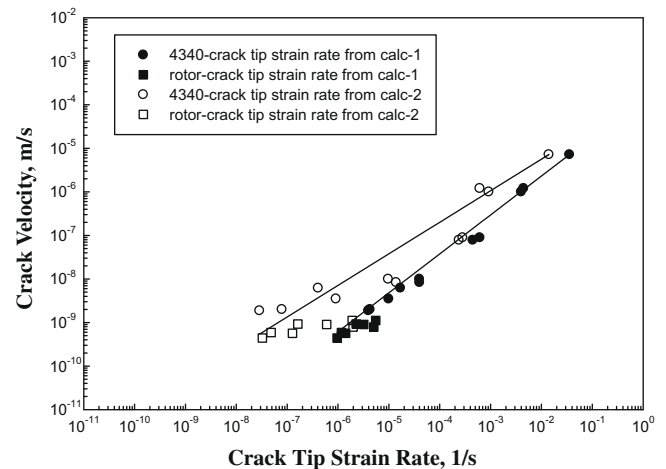


Fig. 8. Average crack velocity plotted as a function of crack tip strain rate (shown in Fig. 5) for both steels. Crack tip strain rate from approach 1 (Eqs. (3) and (4)) and approach 2 (Eq. (5)) have been plotted in this figure. The least square fit parameters are presented in Table 2.

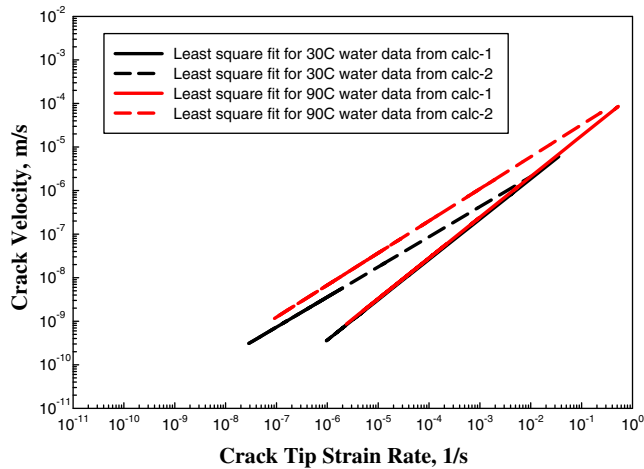


Fig. 9. Comparison of the least square fit data for 30 °C and 90 °C water [15] based on approach 1 (Eqs. (3) and (4)) and approach 2 (Eq. (5)). The least square fit parameters are presented in Table 2.

of plasticity; dimple rupture and slip steps could be clearly seen in these figures. Table 4 presents the rough percentage of intergranular and transgranular fractures on the fracture surface (within the stress corroded region) for samples where fractography was conducted. This table also shows that a significant portion of transgranular fracture was observed on the fracture surface. Moreover, the grain facets appear to be relatively clean in the micrographs in Figs. 10 and 11. These micrographs were obtained near the mid-crack region or near the crack tip. In contrast, the grain facets near the crack initiation point were corroded and covered with some corrosion products. This is shown in Fig. 12 for the rotor steel tested at an applied stress rate of $0.00034 \text{ MPa s}^{-1}$. The markings on the grain facets could be due to the dissolution of the slip steps or the preferential dissolution of grain boundary precipitations.

4. Discussion

4.1. Threshold Stress

The threshold stress for stress corrosion cracking measured in the present work was about 600 MPa for both 4340 and the

3.5NiCrMoV rotor steel. These numeric values correspond to $0.35 \sigma_y$ and $0.47 \sigma_y$ for 4340 and 3.5NiCrMoV rotor steel, where σ_y is the yield stress. Thus 4340 can be considered to be more susceptible to SCC because the onset of SCC occurs at a much lower fraction of σ_y . How does this compare with other systems? SCC in Mg–Al alloys is also associated with hydrogen; the thresh stress was found to be about $0.5 \sigma_y$ so also in the elastic region of applied stress [19,20,38]. In contrast, the initiation stress was found to be just above the yield stress for a range of pipeline steels undergoing SCC in “high pH” carbonate–bicarbonate solution [24]. Furthermore, rock bolt SCC has been found to have a threshold stress close to the ultimate tensile strength [39,40]. This indicates that the threshold stress depends on the particular metal–environment couple.

4.2. Critical applied stress rate and critical crack tip strain rate

In fracture mechanics tests, stress corrosion cracking is not observed for a stress intensity factor below the threshold stress intensity, K_{ISCC} . As shown by Speidel [41], when the stress intensity factor increases above K_{ISCC} towards the plateau stress intensity (K_p), the crack velocity increases rapidly. This is region I of the crack velocity, v , versus K plot. At stress intensity factors above K_p , the crack velocity remains a constant (v_{II}). The results presented in this study, especially the correlation between the applied stress rate and the stress corrosion crack velocity (Fig. 7), indicates that the stress corrosion crack velocity increased with increasing applied stress rates for both steels, until it reached the maximum crack velocity. This maximum crack velocity observed in this study correspond to v_{II} in fracture mechanics tests [16,28,41,46], especially for 4340 in room temperature water [16,28].

Thus, Fig. 7 can be considered to represent the region I of the fracture mechanics tests, an observation similar to that for 90 °C water data [15]. This suggests that in region I of the stress corrosion crack velocity–stress intensity factor plot, the stress corrosion crack velocity is controlled by the crack tip deformation behaviour. Assuming that the stress corrosion crack velocity in region I is indeed controlled by crack tip deformation, the minimum stress corrosion crack velocity observed by Magdowski [16,28] for 4340 steel in room temperature water was $1 \times 10^{-10} \text{ m s}^{-1}$. By extrapolating the least square fit line in Fig. 7 to this minimum crack velocity, the critical applied stress rate below which SCC would not occur in

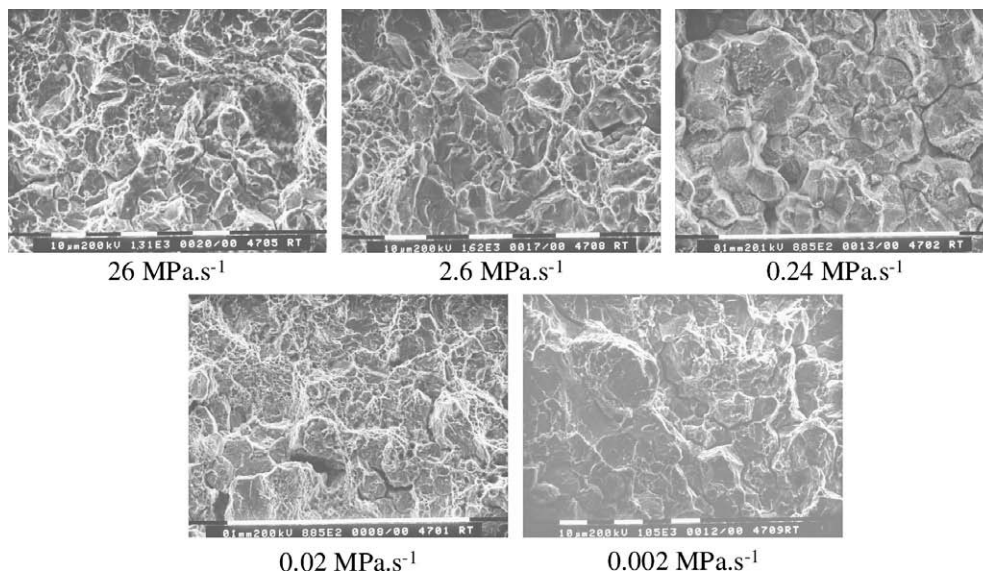


Fig. 10. Representative secondary electron micrographs showing the fracture surface morphology from the LIST experiments in 30 °C water for 4340 steel at various applied stress rates.

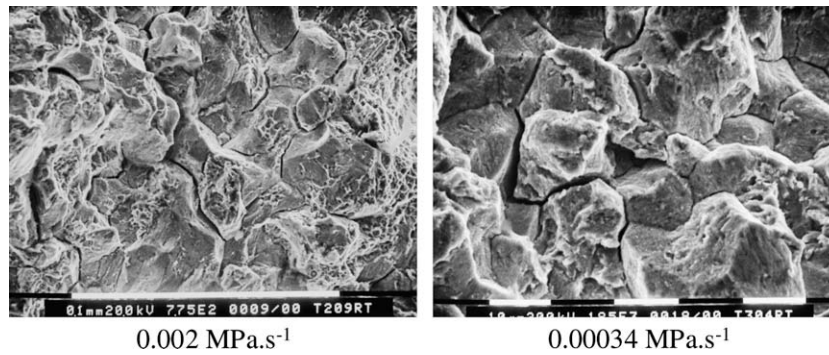


Fig. 11. Representative secondary electron micrographs showing the fracture surface morphology from the LIST experiments in 30 °C water for the rotor steel at two different applied stress rates where there was stress corrosion cracking.

4340 steel can be determined. This extrapolation indicates a value of approximately $2.6 \times 10^{-5} \text{ MPa s}^{-1}$ for the critical applied stress rate.

Using the critical applied stress rate value, the critical applied strain rate below which SCC would not occur can be determined from Fig. 5. By extrapolating the least square fit line in Fig. 5 to this critical applied stress rate of $2.6 \times 10^{-5} \text{ MPa s}^{-1}$, a value of the critical crack tip strain rate of $2.5 \times 10^{-7} \text{ s}^{-1}$ from approach 1 (Eqs. (3) and (4)) and $8.0 \times 10^{-9} \text{ s}^{-1}$ from approach 2 (Eq. (5)) can be obtained. During LIST, the stress state acting at the crack tip varies from plane stress for most of the test to plane strain at final stages of fracture. Hence, the actual critical crack tip strain rate would lie in between these two values and was probably close to $2.5 \times 10^{-7} \text{ s}^{-1}$. The upper limits of the crack tip strain rates, above which SCC could not occur, were 0.35 s^{-1} and $5.1 \times 10^{-6} \text{ s}^{-1}$, corresponding to the applied stress rates of $2.6 \times 10^1 \text{ MPa s}^{-1}$ in 4340 steel and $2.0 \times 10^{-3} \text{ MPa s}^{-1}$ in turbine rotor steel, respectively.

The role of crack tip strain rate in controlling the plateau crack velocity, v_{II} , has been presented in the previous studies [38,42]. The model proposed indicates that there is a limit on the maximum crack tip strain rate that can be attained at the crack tip and this maximum crack tip strain rate determines the plateau crack velocity v_{II} . This maximum crack tip strain rate is dependent on the yield strength of the steel; higher yield strength steels produce higher crack tip stresses, resulting in higher crack tip strain rates and higher v_{II} values. The results from the LIST measurements support the assumption of a maximum in the crack tip strain rate which is dependent on the yield strength of the steel and crack velocities greater than v_{II} could not be produced in either steel.

4.3. Kinetics of SCC

Results presented in the previous sections indicated that the relationship between the stress corrosion crack velocity and the crack tip strain rate calculated from both approaches can be described by the equation: $v = A4\dot{\epsilon}_c^{m4}$, where $A4$ and $m4$ are constants. The value of the exponent was 0.89 and 0.73 for the 30 °C results and these values were similar to those for the 90 °C experiments (Table 3). As discussed, these values were greater than those reported for the SCC of stainless steels (0.3–0.5) in high temperature water [34,37,43,44], but are within the range 0.5–1 reported for sensitized stainless steels in high temperature water [36]. Moreover, typical slopes for $\log v$ versus $\log \dot{\epsilon}$ plots were of the order of 0.5–0.7 for intergranular SCC (IGSCC) and 0.2–0.3 for transgranular (TGSCC) [45]. Thus, the fit parameters from this study are similar to the range reported in the previous studies. Moreover, the fact that the data from this study follow this relationship indicates that the crack tip plasticity controls the film rup-

ture rate and facilitates corrosion at the crack tip. The amount of corrosion after each film rupture event is controlled by the repassivation rate at the crack tip. Thus, the crack tip strain rate and the repassivation rate compete with each other.

The data presented in Fig. 8 show that the stress corrosion crack velocity was dependent on the crack tip strain rate and increased with increasing crack tip strain rate, except for turbine rotor steel at higher crack tip strain rates. Both the 4340 and the turbine rotor steel specimens exhibited similar crack velocities at corresponding crack tip strain rates. In fact, the exponents in Figs. 7 and 8 (as shown in Table 3) have similar values. These observations indicate that the crack velocity was dependent only on the applied stress/strain rate and was independent of the composition of the steels used in the present study. This result is analogous to that observed in region I of the fracture mechanics tests for these steels in high temperature water [41], where the experimental data for these steels lie on the same vertical band. Such observation has also been substantiated by the extensive study conducted by the same group [46]. These observations imply that a similar rate limiting step, independent of steel composition for both steels.

What is the rate limiting step? Scully [47], Newman [48] and others [49–51] suggested that the role of the crack tip strain is to rupture the passive film at the crack tip for an anodic dissolution mechanism. Alternatively, in any mechanism involving hydrogen, the rupture event at the crack tip could be to rupture not a passive film, but merely to rupture a surface film that hinders hydrogen ingress into the material. Thus, the rate of film rupture could be a rate limiting step at both temperatures at both 30 °C and 90 °C. The increase in the crack tip strain rate through the increase in the applied stress rate could increase the film rupture rate and hence accelerate subsequent events. This acceleration would continue until the maximum crack velocity corresponding to the plateau crack velocity, v_{II} , observed in fracture mechanics tests at corresponding temperatures is reached, at which point, the crack tip remains film free and other processes like transportation of the ionic species to and from the crack tip take over as the rate limiting step.

The results presented in Fig. 7 could be explained on the basis of the rate limiting step being film rupture rate. In 4340 steel, the crack velocity increased with increasing applied stress rate, until the maximum crack velocity corresponding to v_{II} is reached. On the basis of the rate limiting step being the film rupture rate, it can be explained that an increase in the applied stress rate causes a corresponding increase in the crack tip strain rate and increase in the film rupture rate leading to increased corrosion and hence crack velocity. However, the results for the turbine rotor steel indicate that the maximum crack velocity observed in the present study was two orders of magnitude less than v_{II} from fracture mechanics tests at room temperature [16,28]. This was probably

Table 4

Percentage of intergranular and transgranular failure at the fracture face in the two steels at different applied stress rates where stress corrosion cracking was observed. These percentages correspond to the regions from the stress corrosion cracking only and do not include the ductile overload failure regions. N/A – data not available.

Steel	Applied stress rate, MPa s ⁻¹	Percentage of intergranular failure	Percentage of transgranular failure
4340	26.0000	50	50
	2.6000	55	45
	0.24000	50	50
	0.02080	60	40
	0.00208	70	30
	0.00034		
Rotor	0.00208	60	40
	0.00034	70	30
	0.00020	N/A	N/A

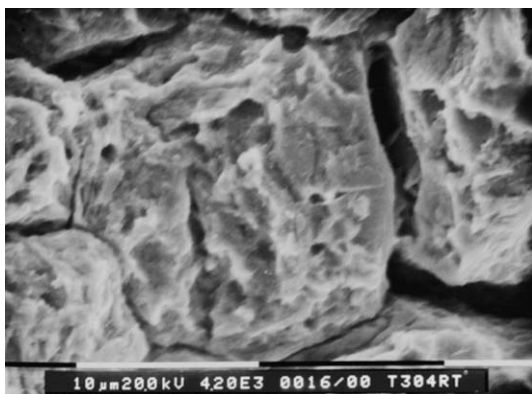


Fig. 12. Secondary electron micrograph for the rotor steel specimen at an applied stress rate of 0.00034 MPa s⁻¹. This micrograph was obtained near crack initiation and showed corroded grains.

due to the fact that some other process, besides the film rupture rate, is active at the crack tip and controls the crack growth rate. This process could be independent of the applied stress rate, which could explain why the crack velocity did not increase much with the increase in the applied stress rate. Thus, the rate limiting step at higher applied stress rates could be different for 4340 and rotor steels. Moreover, at higher applied stress rates, the rate limiting process for the rotor steel is too slow to cause failure by SCC and hence, stress corrosion was not observed at applied stress rate higher than 0.002 MPa s⁻¹.

Though it appears that there is good evidence for the rate limiting step being film rupture rate and being the same for tests conducted in 30 °C and 90 °C water (based on the similar exponents observed for least square fit data), the actual mechanism of cracking could be different at these two temperatures. Magdowski [16,28] reports that the crack growth rate – temperature plots have different slopes in the high (approximately above 60 °C) and low temperature regions. The slope in the low temperature region was consistent with the Hydrogen Embrittlement mechanism (HE) and the high temperature region's slope was consistent with the Anodic Dissolution (AD) mechanism. Their work was supported by the work of Rieck et al. [17,52]. The present study could not reveal which of these two mechanisms operate in 30 °C water. The suggestion of HE to be the mechanism of cracking would agree with the results presented in this study, as the rate of hydrogen production is dependent on the rate of corrosion at the crack tip,

which in turn depends on the rate of film rupture and hence on the crack tip strain rate and the applied stress rate.

4.4. Fractography

Figs. 10 and 11 indicate that the fracture morphology was intergranular in both steels, with large transgranular regions present within the intergranular region. This suggests the presence of a preferential crack path along the prior austenite grain boundaries. The role of grain boundary segregants, which have been reported as a possible cause of preferential attack, has been discounted by others [16,28,41]. Rieck [17,52] presented a model for the intergranular cracking, which proposes that the crack path is defined by the surface where most dislocations meet. Some of the micrographs presented in Figs. 10 and 11 show the slip steps on some of the grain facets. The slip steps appear to be wavy, which suggests that the slip cannot concentrate on one plane. The next obstacle the dislocations meet is the grain boundary. In low alloy steels, the prior austenite grain boundaries remain high angle grain boundaries and present a more significant obstacle to dislocation motion than the low angle twin boundaries found in martensite. This pile up of dislocations at the prior austenite grain boundaries produce concentration ledges and lead to dissolution of these ledges, causing cracking to be intergranular.

Another possible mechanism of intergranular cracking is the growth and the rupture of oxide films, as proposed by Atrens and Wang [27]. Using environmental SEM (ESEM), they have observed that, for the 4340 steel in distilled water, oxide film was found to form on the surface of 4340 steel specimen after immersion in water. Applied stress was found to accelerate the oxide growth and the presence of small cracks within the oxide layer provided the pathway for the water to reach the bare metal. If the cracks are along the grain boundaries, then initiation along the grain boundaries have been observed. Corrosion at the exposed cracks appeared to be limited by the oxide healing process, thus the formation of cracks and the crack healing appeared to be competing processes occurring on the sample surface. If the intergranular penetration is faster than the crack healing process, then crack growth was observed. However, if the crack penetration was slower than the crack healing process, then shallow cracks were observed. In some of their experiments, they have also observed crack initiation from corrosion pits.

In the present study, the intergranular cracking observed on 4340 and rotor steel specimens could be due to the dislocations-assisted film rupture or due to the cracking of oxides along the grain boundaries. It is also possible that the build-up of dislocations could result in the cracking of oxide film and when this occurs along a suitably oriented grain boundary, crack initiation and propagation would occur.

5. Conclusions

LIST experiments were performed on as-quenched 4340 and 3.5NiCrMoV turbine rotor steel specimens in 30 °C distilled water. The experimental results from this study indicate that:

- (1) For the 4340 steel specimens, there was stress corrosion cracking at all applied stress rates, though some specimens tested at stress rates of 2.08 and 20.8 MPa s⁻¹ failed in a ductile manner. For this steel, the fracture stress decreased slightly with decreasing applied stress rate until 0.02 MPa s⁻¹ and decreased significantly with further decrease in the applied stress rate. The threshold stress decreased slightly with decreasing applied stress rate.

- (2) For the rotor steel, there was no stress corrosion cracking at applied stress rates greater than 0.002 MPa s^{-1} . Where stress corrosion was observed, the fracture stress remained essentially constant with increasing applied stress rate and the threshold stress was found to decrease with the decrease in the applied stress rate.
- (3) For 4340, the stress corrosion crack velocity increased with increasing applied stress rate until it reached a maximum stress corrosion crack velocity, corresponding to the plateau stress corrosion crack velocity measured in fracture mechanics tests in room temperature water [16,28].
- (4) The stress corrosion crack velocity was dependent on the applied stress rate and the crack tip strain rate. It was independent of the steel composition, indicating a similar rate limiting step, independent of steel composition for both steels.
- (5) Exponents of the least square fit data were similar for both 30°C and 90°C water experiments, indicating that the same rate limiting step could be operating at both temperatures.
- (6) Fracture surface morphology was mixed mode consisting of some intergranular fracture, significant transgranular regions and a significant amount of plasticity. In addition, the applied stress rate did not influence the fracture morphology.
- (7) Crack initiation and propagation could be due to the build-up of dislocations along the grain boundaries or due to the formation of cracks in the oxide layer at grain boundary regions or a combination of both processes.

Acknowledgments

The authors would like to acknowledge Professor Leo Lau, Director, Surface Science Western, The University of Western Ontario, London, Ontario, Canada for many useful discussions and for his kind encouragement throughout this work.

References

- [1] R.P. Gangloff, Hydrogen-assisted cracking, in: I. Milne, R.O. Ritchie, B. Karihaloo (Eds.), *Comprehensive Structural Integrity, Environmentally Assisted Failure*, vol. 6, 2003, pp. 31–101.
- [2] J.M. Hodge, I.L. Mogford, *Proc. Inst. Mech. Eng.* 96 (1979) 193.
- [3] D. Kalderon, *Proc. Inst. Mech. Eng.* 186 (1972) 341.
- [4] C. Liu, D.D. Macdonald, *J. Press. Vess. Technol.* 119 (1997) 393.
- [5] H.L. Li, K.W. Gao, L.J. Qiao, Y.B. Wang, W.Y. Chu, *Corrosion* 57 (2001) 295–299.
- [6] N. Eliaz, A. Shachar, B. Tal, D. Eliezer, *Eng. Fail. Anal.* 9 (2002) 167–183.
- [7] W.Y. Maeng, J.H. Lee, U.C. Kim, *Corros. Sci.* 47 (2005) 1876–1895.
- [8] W.Y. Maeng, D.D. Macdonald, *Corros. Sci.* 50 (2008) 2239–2250.
- [9] S.P. Lynch, *Corrosion 2007, NACE – International Corrosion Conference Series*, 2007, p. 074931–0749355.
- [10] T. Nakayama, *Welding Int.* 21 (2007) 89–94.
- [11] E. Villalba, A. Atrens, *Eng. Fail. Anal.* 15 (2008) 617.
- [12] B.Y. Fang, A. Atrens, J.Q. Wang, E.H. Han, Z.Y. Zhu, W. Ke, *J. Mat. Sci.* 38 (2003) 127–132.
- [13] A. Turnbull, S. Zhou, *Corros. Eng. Sci. Technol.* 38 (2003) 177–191.
- [14] S. Zhou, NPL Report DEPC-MPE 033, 2007, p. 33.
- [15] S. Ramamurthy, A. Atrens, *Corros. Sci.* 34 (1993) 1385–1402.
- [16] R.M. Magdowski, *Stress Corrosion Cracking of Low Alloy Steel in Water*, D. Tech. Sc. Thesis, Swiss Federal Institute of Technology, Zurich, 1987.
- [17] R.M. Rieck, A. Atrens, I.O. Smith, *Met. Trans.* 20A (1989) 889–895.
- [18] A. Atrens, C.C. Brosnan, S. Ramamurthy, A. Oehlert, I.O. Smith, *Meas. Sci. Tech.* 4 (1993) 1281–1292.
- [19] N. Winzer, A. Atrens, W. Dietzel, V.S. Raja, G. Song, K.U. Kainer, *Mat. Sci. Eng. A* 488 (2008) 339–351.
- [20] N. Winzer, A. Atrens, W. Dietzel, G. Song, K.U. Kainer, *Mat. Sci. Eng. A* 472 (2008) 97–106.
- [21] J.Q. Wang, A. Atrens, *Eng. Fail. Anal.* 11 (2004) 3–18.
- [22] J. Wang, A. Atrens, *Corros. Sci.* 45 (2003) 2199–2217.
- [23] A. Atrens, A. Oehlert, *J. Mat. Sci.* 33 (1998) 783–788.
- [24] Z.F. Wang, A. Atrens, *Met. Mat. Trans A* 27A (1996) 2686–2691.
- [25] A. Oehlert, A. Atrens, *J. Mat. Sci.* 33 (1998) 775–781.
- [26] J. Salmond, A. Atrens, *Scripta Metall. Mat.* 26 (1992) 1447–1450.
- [27] A. Atrens, Z.F. Wang, *J. Mat. Sci.* 33 (1998) 405–415.
- [28] R.M. Magdowski, in: P.J. Uggowitzer (Ed.), *Moderne Stahle*, Zurich, 1987, pp. 107–140.
- [29] H.G. Nelson, D.P. Williams, in: R.W. Staehle, J. Hockmann, R.D. McCright, J.E. Slater (Eds.), *Proc. NACE-5, Stress Corrosion Cracking and Hydrogen Embrittlement of Iron Base Alloys*, Houston, 1977, pp. 390–404.
- [30] G.W. Simmons, P.S. Pao, R.P. Wei, *Met. Trans.* 9A (1978) 1147–1158.
- [31] J.D. Gates, A. Atrens, I.O. Smith, *Z. Werkstoff.* 18 (1987) 165–170.
- [32] J. Congleton, T. Shoji, R.N. Parkins, *Corros. Sci.* 25 (1985) 633–650.
- [33] J.M. Silcock, *Corros. Sci.* 21 (1981) 723–730.
- [34] F.P. Ford, P.W. Emigh, *Corros. Sci.* 25 (1985) 673–692.
- [35] F.P. Ford, P.L. Andresen, *Proc. Corrosion 87, NACE*, Houston, 1987, pp. 83/1–83/19.
- [36] D.P.G. Lidbury, in: R.P. Gangloff (Ed.), *Embrittlement by the Localized Crack Environment*, The Metallurgical Society – AIME, Warrendale, PA, 1983, pp. 149–172.
- [37] P.S. Maiya, W.J. Shack, in: R.P. Gangloff (Ed.), *Embrittlement by the Localized Crack Environment*, The Metallurgical Society – AIME, Warrendale, PA, 1983, pp. 199–209.
- [38] N. Winzer, A. Atrens, W. Dietzel, G. Song, K.U. Kainer, *Metallurgical and Materials Transactions A* 39 (2008) 1157–1173.
- [39] E. Gamboa, A. Atrens, *Eng. Fail. Anal.* 10 (2003) 521–558.
- [40] E. Gamboa, A. Atrens, *Eng. Fail. Anal.* 12 (2005) 201–225.
- [41] M.O. Speidel, in: M.O. Speidel, A. Atrens (Eds.), *Proc. Corrosion in Power Generating Equipment*, Plenum, New York, 1984, pp. 85–130.
- [42] R.M. Rieck, A. Atrens, S. Ramamurthy, J.D. Gates, I.O. Smith, in: R.P. Gangloff, M.B. Ives (Eds.), *NACE-10 Environment Induced Cracking of Metals*, NACE, Houston, 1990.
- [43] F.P. Ford, Report No. 81CRD125, General Electric Company, New York, 1981.
- [44] P.S. Maiya, *J. Press. Vess. Technol.* 109 (1987) 116–123.
- [45] S.A. Serebrinsky, G.S. Duffo, J.R. Galvele, *Corros. Sci.* 41 (1999) 191–195.
- [46] R.M. Magdowski, M.O. Speidel, *Metall. Trans.* 19A (1988) 1583–1596.
- [47] J.C. Scully, *Corros. Sci.* 20 (1980) 997–1016.
- [48] J.F. Newman, *Corros. Sci.* 21 (1981) 487–503.
- [49] D.A. Vermilyea, in: R.W. Staehle, J. Hockmann, R.D. McCright, J.E. Slater (Eds.), *Stress-Corrosion Cracking and Hydrogen Embrittlement of Iron-Base Alloys*, NACE, Houston, 1977, pp. 208–217.
- [50] F.P. Ford, P. Andresen, in: P. Marcus (Ed.), *Corrosion Mechanisms in Theory and Practice*, Marcel Dekker, New York, 2002, pp. 605–642.
- [51] Z. Lu, T. Shoji, *J. Press. Vess. Technol. (Trans. ASME)* 128 (2006) 318–327.
- [52] R.M. Rieck, A. Atrens, S. Ramamurthy, J.D. Gates, I.O. Smith, in: *International Conference on Environment Induced Cracking*, Kohler, Wisconsin, USA, October 1988.